RESEARCH ARTICLE

Key Points:
- Circulation around both islands is dominated by westward propagating features
- The predominant time scale of variability of currents and SSH is 60 days
- There is local generation of eddies in the lee of the islands due to topography

Correspondence to:
S. Pous,
pous@mnhn.fr

Circulation around La Réunion and Mauritius islands in the south-western Indian Ocean: A modeling perspective

Stéphane Pous[1,2,3], Pascal Lazure[4], Gaël André[5], Franck Dumas[4], Issufo Halo[2,6], and Pierrick Penven[3,7]

[1]LOCEAN Laboratory, Sorbonne Universités (UPMC, Univ PARIS 06)-CNRS-IRD-MNHN, Paris, France, [2]Department of Oceanography, University of Cape Town, Cape Town, South Africa, [3]LMI ICEMASA, IRD, University of Cape Town, Cape Town, South Africa, [4]Institut Francais de Recherche pour l'Exploitation de la Mer, Plouzané, France, [5]Altran Ouest, Brest, France, [6]Nansen-Tutu Centre for Marine Environmental Research, University of Cape Town, Cape Town, South Africa, [7]Laboratoire de Physique des Océans, Plouzané, France
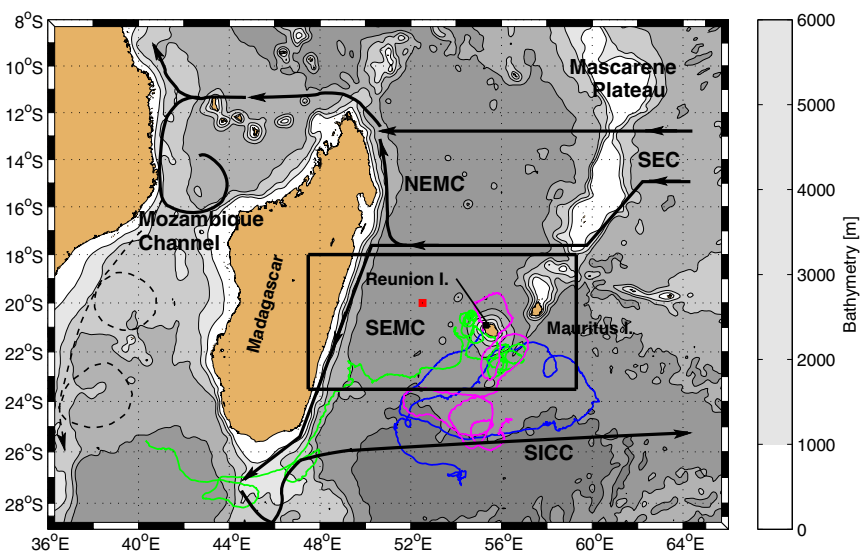
Abstract The objective of this study is to document the circulation in the vicinity of La Réunion and Mauritius islands, i.e., within 500 km offshore, on the intraseasonal time scale, using a high-resolution realistic modeling strategy. The simulated sea level anomalies, water mass properties, and large-scale circulation compare favorably with satellite and in situ observations. Our high-resolution simulation suggests that the currents around the islands are maximal locally, oriented southwestward, to the southeast of both islands which is not visible in low-resolution satellite observations. It also highlights the high degree of variability of the circulation, which is dominated by westward propagating features. The predominant time scale of variability is 60 days. This coincides with the period of a barotropic mode of variability confined to the Mascarene Basin. The characteristics of the westward propagating anomalies are related to baroclinic Rossby waves crossing the Indian Ocean but only in the long-wave resting ocean limit. Tracking those anomalies as eddies shows that they also have a meridional tendency in their trajectory, northward for cyclones and southward for anticyclones, which is consistent with previous studies. Sensitivity experiments suggest that they are predominantly advected from the east, but there is also local generation in the lee of the islands, due to interaction between the circulation and topography.

1. Introduction

La Réunion and Mauritius islands (hereafter RI and MI) are situated in the south-western Indian Ocean (SWIO), at the south-western tip of the Mascarene Plateau, to the east of Madagascar (Figure 1). They host approximately 2 million citizens and a wide variety of marine ecosystems in their vicinity, which are at the center of international research programs (Agulhas and Somali Current Large Marine Ecosystems Project (ASCLME), Western Indian Ocean Marine Science Association (WIOMSA)). Documenting the circulation in the vicinity of the islands, which has not been done yet, is likely to contribute to the research activities on the marine life, provide a reference for risk management strategies (in case of marine pollution) and yield boundary conditions to coastal studies around the islands. The motivation of this study is to provide such documentation using a realistic high-resolution modeling strategy.

The circulation and water masses in the SWIO have already been documented [*Morales et al.*, 1996; *Stramma and Lutjeharms*, 1997; *de Ruijter et al.*, 2005]. The main circulation feature is the South Equatorial Current (SEC) that is most intense at the surface but reaches up to 1400 m depth, and forms the northern boundary of the basin-wide anticyclonic Indian subtropical gyre which carries 50–55 Sv westward between 10°S and 20°S [*Schott and McCreary*, 2001; *New et al.*, 2007]. When this current reaches the Mascarene Plateau, which consists of a series of ridges separated by shallow banks or "shoals," at about 60°E, the inflow splits into two cores [*New et al.*, 2007]. The northern core passes between 10°S and 14°S, to the north and over a narrow sill at the middle of the plateau, and the second passes to the south, near Mauritius between 17°S and 20°S. On reaching Madagascar, these cores contribute to the Northeast and Southeast Madagascar Currents (NEMC and SEMC) [*Schott and McCreary*, 2001]. The NEMC transports about 30 Sv northward around Madagascar, supplying the Mozambique Channel and the East African Coastal Current. The SEMC transports about 20 Sv southward along Madagascar. At the southern tip of Madagascar, part of the SEMC splits into a

sequence of eddies and dipoles that migrate to the African coast [*de Ruijter et al.*, 2005]. The remaining ret-

Figure 1. Bathymetry of the southwestern part of the Indian Ocean. Black arrows locate the main currents, namely the South Equatorial Current (SEC), the Northeast Madagascar Current (NEMC), the Southeast Madagascar Current (SEMC), and the South Indian Ocean Counter-current (SICC). Color lines depict trajectories of three 15 m depth drifters launched near La Réunion Island in December 2010 and March 2011. The black square indicates the position of the tide-gauge station "Pointe des galets." The red square indicates the position of the ICM3 6a current meter. The box shows the limits of the regional model.

roflects and feeds a shallow eastward jet [*Siedler et al.*, 2006] identified as the South Indian Ocean Counter-current (SICC) [*Palastanga et al.*, 2006]. A wide range of water masses are found in the SWIO, the SEC acting as a barrier, in the upper ocean, between water masses of southern and northern origin, essentially contrasted by their salinity [*Schott and McCreary*, 2001; *New et al.*, 2007]: Subtropical Surface Water (STSW), Sub-Antarctic Mode Water (SAMW), and Antarctic Intermediate Water (AAIW) on the southern side of the SEC, Arabian Sea High Salinity Water and Red Sea Water on its northern side. Tropical Surface Water is evident as a fresh surface layer carried westward by the SEC in the upper 50–100 m. At depth, to the west of the Plateau, are found North Indian Deep Water and Antarctic Bottom Water.

The circulation in the vicinity of RI and MI, within 500 km off the coasts, remains largely unknown. Three drifting buoys launched near the coast of RI (technical details given hereafter) exhibited circular motions of various spatial scale and rapidly drifted away from each other (Figure 1). This proves the existence of eddies in the vicinity of the islands, and illustrates the high degree of variability of the circulation around RI. One buoy was trapped in small-scale structures (30–50 km) in the vicinity of RI, before travelling fast to Madagascar and the Mozambique Channel (green line). Another drifted as far as 200 km away from RI before coming back to the coastal area (blue line). Understanding better these types of motion is crucial to clarify marine ecosystem dynamics, such as connectivity questions. A first step is to establish more clearly the circulation in the vicinity of the islands, both the temporal mean and the typical anomalies, which is the objective of this paper.

According to previous studies, sea level variability in the SWIO is dominated by westward propagating anomalies, about 4–5 per year [*Schouten et al.*, 2002a; *Palastanga et al.*, 2007], but the nature and the origin of these anomalies remain unclear. *Birol and Morrow* [2001, 2003] and *Schouten et al.* [2002b] attributed them to Rossby waves, originating from the boundary region off West Australia, while *Quartly et al.* [2006] considered them more likely to be a train of propagating eddies. Following *Chelton et al.* [2007, 2011], it is likely that much of the mesoscale variability near RI and MI consists of nonlinear eddies propagating westward at the phase speed of baroclinic Rossby waves. Besides, *Palastanga et al.* [2007] and recently *Jia et al.* [2011] suggested that these mesoscale anomalies are due to baroclinic instability processes associated with the surface eastward flowing SICC and the underlying westward flowing SEC system. Notwithstanding, *Weijer* [2008] hypothesizes that the westward propagating anomalies observed in the deep Mascarene

Basin [*Warren et al.*, 2002] are related to a local barotropic Rossby basin mode. Rather than reconciling all these interpretations, our realistic simulation gives evidence for each of those, which confirms the complexity of ocean dynamics in this region.

Direct observations of the circulation in the vicinity of RI and MI are sparse. Satellite observations provide valuable information on the upper ocean currents, but at a resolution that may not be sufficient to allow for a proper identification of mesoscale processes relevant for the circulation. Hence, we developed a modeling strategy to reproduce, in the most realistic way, the circulation in the vicinity of the islands, from January 1994 to December 2009. Our focus is on the intraseasonal time scale and on spatial mesoscales. We first describe all available observations and the model configuration (section 2). After validating the simulated outputs (section 3), we characterize the circulation around both islands (section 4). We then focus on the processes of variability that imprint the synoptic circulation, through a Eulerian perspective and via the tracking of eddies on both observed and simulated data sets (section 5). The summary and discussion of the results are given in section 6.

2. Material and Methods

2.1. Observed Data Sets

Maps of Absolute Dynamic Topography (hereafter MADT) data used in the present study has been produced by Ssalto/Duacs and distributed by AVISO, with support from CNES (http://www.aviso.oceanobs.com/duacs/). MADT data are obtained by combining measured sea level anomaly data from different altimeter products (Topex/Poseidon, ERS, Envisat, and Jason altimeters) with mean dynamic topography. MADT data correspond to the global AVISO "ref" delayed time products, from 1992 to 2009. The spatial resolution of the gridded product is $1/3°$ and the temporal resolution is 7 days.

Sea surface height (hereafter SSH) is also measured by the tide-gauge station "Pointe des galets" located at $55.3°E$; $20.9°S$ on the northwest coast of RI (see Figure 1, data available on http://refmar.shom.fr). This station provides measurements from 1979 to 2010, but there are gaps in the time series.

ARGO profile data are used to analyze the vertical structure of thermohaline properties in the vicinity of RI and MI. ARGO floats provide measurements of pressure, temperature (T), and salinity (S) down to 2000 m depth. These data were collected and made freely available by the International Argo Project and the national initiatives that contribute to it (http://www.argo.net). Observations were selected in the area of interest, from 2003 to 2009 and amount to a total of 1618 profiles. Salinity at 10 m depth was taken from IFREMER/LOS Mixed Layer Depth Climatology website (www.ifremer.fr/cerweb/deboyer/mld).

The daily Optimally Interpolated (OI) SST product, derived from the Tropical Rainfall Measuring Mission (TRMM) Microwave Imager (TMI) [*Kummerow*, 2000], at $1/4°$ resolution is employed for validation of simulated SST. Horizontal resolution of this data set is relatively low, but the measure is not affected by the presence of clouds, which is particularly important in tropical latitudes. The product is provided by the Remote Sensing Systems and is available since 1998.

The Ocean Surface Current Analysis—Realtime (OSCAR, http://www.oscar.noaa.gov) [*Bonjean and Lagerloef*, 2002] project provides 5 day resolution gridded ($1/3°$) estimates of the average current from the surface to 15 m depth. The formulation combines geostrophic currents estimated from satellite-derived sea level together with the wind-driven (Ekman) contribution.

Time series of velocity from a current meter moored in western Mascarene Basin ($20°S$; $52.517°E$) at 2473 m depth is used in this study. This mooring was deployed on 30 May 1995 and recovered on 19 January 1997 as part of a WOCE project (designated ICM3). This current meter is identified by mooring 6a by *Warren et al.* [2002]. The ICM3 records are available from the WOCE Current Meter Data Assembly Center at Oregon State University.

Surface currents were indirectly measured with three Technocean (http://www.technocean.com) SVP ARGOS drifters equipped with holey socks centered at 15 m. The drifters were deployed from a fishing boat around the western coast of RI in December 2010 and March 2011. The data were quality-checked and interpolated at 30 min intervals. The first drifter (No. 102032) sampled from 8 December 2010 to 31 August

2011. The second drifter (No. 102033) sampled from 7 December 2010 to 24 July 2011 and the third drifter (No. 102037) sampled from 25 March to 21 August 2011.

2.2. Regional Circulation Model

Modeling was performed using the MARS-3D (3-D hydrodynamic Model for Applications at Regional Scales). The MARS-3D model has been fully described by *Lazure and Dumas* [2008]. It is a finite difference, mode splitting model with novel coupling of the barotropic and baroclinic modes within a sigma generalized vertical coordinate framework. Inside the domain, horizontal mixing coefficients are constant with a value of about 6 m^2 s^{-1}, increasing in a 10-cell-wide sponge layer up to 300 m^2 s^{-1}. Vertical turbulent coefficients are calculated with a $k-\epsilon$ two equations closure model [*Umlauf and Burchard*, 2003]. The model extends from 47.5°E to 59.3°E and from 23.5°S to 18°S (Figure 1), thus including the Réunion and Mauritius islands with a maximum depth of 5500 m. The horizontal and temporal resolution are, respectively, 2 km and 100 s. Thirty sigma vertical levels are considered and refined near the surface using stretching parameters: $\theta=6$, $b = 0$, and $h_c=9$ [*Song and Haidvogel*, 1994]. This grid spacing in sigma generalized coordinate corresponds to a vertical resolution ranging from 32 cm to 6.1 m for the surface layer and from 3.3 to 936 m for the bottom. The bathymetry has been built from in situ data [FOREVER and ERODER1 cruises, *Le Friant et al.*, 2011], combined with global bathymetry SRTM30_PLUS [*Becker et al.*, 2009] in areas where in situ data were missing. This bathymetry represents realistically the volcanic islands, Mascarene plateau and the shallow at 54.15°E; 19.7°S. Due to the strongly varying bathymetry, σ-coordinate system solutions exhibit an intrinsic error in the horizontal pressure gradient term [*Shchepetkin and McWilliams*, 2003]. In order to minimize the error in the computation of the internal pressure gradient, the bathymetry is smoothed using a Shapiro filter [*Sikirić et al.*, 2009] to keep the topographic parameter: $r=\frac{\nabla h}{2h}$ lower than 0.2. Moreover, particular attention was paid to the formulation of the internal pressure gradient in order to reduce the truncation errors in the horizontal pressure gradient. We used the formulation proposed by *Marsaleix et al.* [2009] where the buoyancy parameter is evaluated according to a reference density profile computed as the time-average of density around RI. This formulation, combined with smoothing of the bathymetry, tends to drastically reduce these truncation errors.

Surface atmospheric forcing is obtained from ERA-Interim atmospheric reanalysis [*Dee et al.*, 2011] at 6 h time step. The ERA-Interim reanalysis provides 10 m wind, 2 m air humidity, and 2 m air temperature to compute turbulent air/sea fluxes during model integration, using the bulk formula proposed by *Large and Yeager* [2004]. Downward short-wave and long-wave radiative fluxes and precipitation are also provided by ERA-Interim.

The initial conditions and lateral open-boundary fields are provided by the GLobal Ocean ReanalYsis and Simulation [*Ferry et al.*, 2012]. GLORYS2V1 is a global ocean and sea-ice eddy permitting reanalysis over the altimetric era (1993–2009). This reanalysis is based on the NEMO Ocean General Circulation Model (OGCM) [*Madec*, 2008] at 1/4° horizontal resolution and 75 vertical levels, forced with ERA-Interim surface atmospheric parameters and assimilating sea surface temperature, in situ profiles of temperature and salinity and along-track sea level anomaly observations. Here we used the 1 day averages of GLORYS2V1 outputs.

The initial condition is a 3-D interpolation of the fields of GLORYS2V1 for 1 January 1993. At lateral open boundaries, surface elevation is prescribed with a Dirichlet condition (which specifies the values of the model surface elevation), while mixed conditions are applied on temperature and salinity (an upstream condition for outgoing scalar fluxes and relaxation to GLORYS2V1 for incoming fluxes). This implies that the external fields are advected into the smaller domain during inflow situations only. Moreover, in a band of 10 grid steps, temperature and salinity are relaxed toward the values obtained from GLORYS2V1 using a constant coefficient, thus introducing a time relaxation scale of approximately 15 days. A zero-gradient condition is applied to baroclinic and barotropic velocities at open boundaries. At the open boundary, surface elevation computed from the main tidal components from the FES2004 model [*Lefevre et al.*, 2002; *Lyard et al.*, 2006] is added to the prescribed one from GLORYS2V1. Particular attention has been given to the proper representation of the SEC by GLORYS2V1 (not shown), as it directly forces the model eastern boundary.

This simulation (hereafter MARS) was performed from the 1 January 1993 to 31 December 2009. The model solution quickly adjusts to the initial stratification and the model reaches a statistical equilibrium after a

spin-up of a few months. Thus, the first year of the simulation has not been taken into account in the following analysis.

Additional experiments were performed to investigate the origin of mesoscale processes in the region. Among all possible driving mechanisms, we focused on three possible candidates: (i) the advection of mesoscale processes through the open boundaries, the local generation of mesoscale processes, (ii) in the wake of the islands, and (iii) due to wind forcing. To evaluate the respective contribution of each of these mechanisms, we ran the following experiments: OBCCLIM with monthly climatological forcing at the lateral open boundaries (monthly means of GLORYS2V1 outputs were averaged over the period 1993–2009), OBCCLIM-NOISL with climatological forcing at the lateral open boundaries and with an idealized version of the bathymetry that does not reproduce RI and MI, NOWIND with no wind forcing (except via air-sea heat fluxes), and WRF with high-resolution atmospheric forcing. WRF experiment uses the Weather Research and Forecasting model to downscale the ERA-interim solution. All sensitivity experiments were run from January 1993 to December 2000 (except WRF that was only run for the year 2007), over a smaller domain (from 51°E to 59.3°E and from 23.5°S to 18°S). Hence, we performed a new reference experiment, named REF, for the same domain and time period (all other parameters identical to MARS simulation). As a result, REF is the same as MARS but in a smaller region and for a shorter time period. We also ran experiment REF-NOISL (in which the boundary conditions are those of the reference experiment and the topography has the islands cut out) to evaluate the impact of RI and MI on mesoscale processes advected through the open boundaries. To prepare the bathymetry of NOISL experiments, all points in the vicinity of RI and MI where the bathymetry is shallower than 3800 m have been masked, then filled with new bathymetry values extrapolated from the nearby nonmasked values.

All model outputs were recorded on a 3 day time step using a Demerliac filter [*Demerliac*, 1974], that is expected to filter out semidiurnal, diurnal, and inertial frequencies.

2.3. Methods

The zonal (u) and meridional (v) components of the geostrophic velocities are derived from SSH through $u = -\frac{g}{f}\frac{\partial \eta}{\partial y}$ and $v = \frac{g}{f}\frac{\partial \eta}{\partial x}$ where g is gravity, f is Coriolis parameter, and η is SSH (from altimetry or model outputs). Eddy Kinetic Energy (EKE) is calculated from SSH-derived geostrophic velocities. EKE is defined as $\frac{1}{2}(u'2 + v'2)$, where $u' = u - \bar{u}$ and $v' = v - \bar{v}$; $\bar{u}$ and $\bar{v}$ being the temporal mean over the whole period.
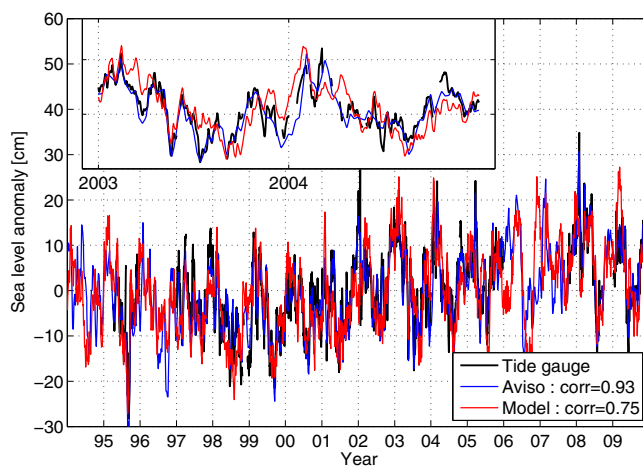
To quantify the relationship between observed EKE and eddy changes, an eddy-detection scheme, combining the Okubo-Weiss and closed-contour methods, was implemented. An evaluation of different eddy-detection methods is provided by *Souza et al.* [2011]. Here the detection is improved by combining two methods, reducing the sensitivity to the choice of parameters, resulting in a more robust eddy detection [*Halo et al.*, 2014]. The eddy-tracking algorithm follows eddies by minimizing a generalized distance in parameter space from one frame to the subsequent frame [*Penven et al.*, 2005; *Souza et al.*, 2011]. Only eddies with a life time greater than 30 days are considered in the present study.

Comparison between observed and simulated data sets may be biased if the spatial sampling is not similar. We computed a decimated version of the model output, by selecting 1 data every 16 model grid points in latitudinal and longitudinal directions (model resolution is 2 km while we used 1/3° AVISO products). The decimated REF outputs are mentioned as MARS-dec in the following.

3. Model Validation

We first compare MARS sea level anomalies (hereafter SLA) at the tide-gauge station "Pointe des galets" with tide-gauge and satellite observations (AVISO). SLA are calculated from the absolute sea surface height (tide-gauge and AVISO MADT for observations, and MARS model outputs), by subtracting the temporal mean over the period 1994–2009. Simulated and tide-gauge time series are 3 day Demerliac filtered to remove the tidal signal. Besides, AVISO and simulated time series are corrected using ERA-Interim atmospheric pressure to include the contribution of atmospheric pressure anomalies. The three time series are comparable at all frequencies (Figure 2). Subannual periods are characterized by the occurrence of 4–6 events every year (as illustrated in 2003 and 2004) in addition to a seasonal modulation (SLA are generally positive in austral summer and fall and negative in winter and spring). Although the peaks are not exactly superimposed in the three time series, they all exhibit similar type of variability at this time scale. There is
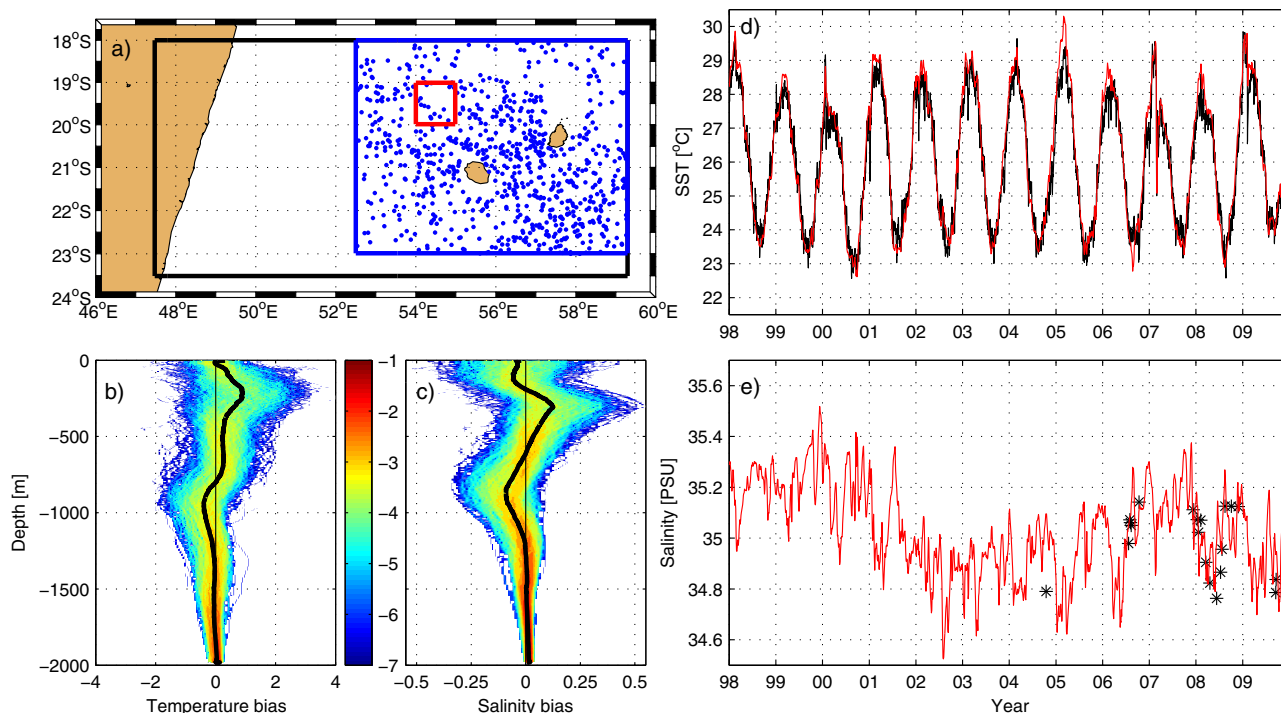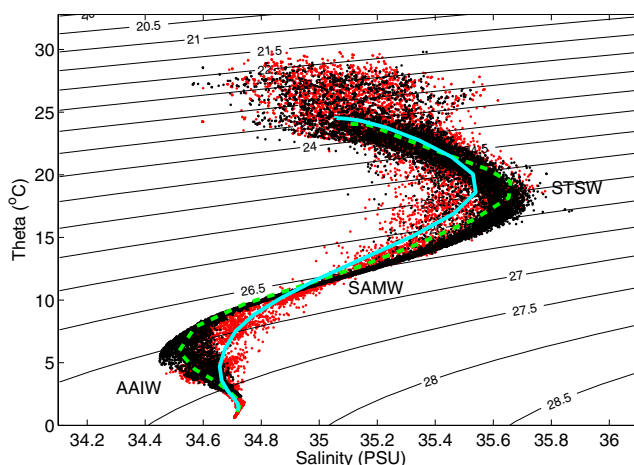
Figure 2. Time series of 3 days Demerliac filtered sea level anomalies at the tide-gauge station "Pointe des galets" from tide-gauge observations (black), AVISO (blue), and model simulation (red), with close-up on years 2003 and 2004 (inset).

also substantial variability at interannual to decadal time scale, with a decrease from 1994 to 1999 and an increase from 1999 to 2002, visible in MARS, tide-gauge, and AVISO. Finally, correlation between simulated and observed time series reaches 0.75 for both observed data sets, which confirms the model ability in reproducing the variability in SSH in the vicinity of RI. Note that the correlation between tide-gauge and AVISO observations is 0.93, showing the ability of AVISO in capturing this variability despite its low resolution.

Simulated water masses in the vicinity of RI and MI are collocated, in space and time, with ARGO profiles (Figures 3a–3c and 4). The principal water masses are reproduced by the model: STSW characterized by a salinity maximum (located at about 250 m depth); SAMW with temperature ranging from 8 to 15°C and AAIW characterized by a salinity minimum (located between 800 and 1500 m depth). The main discrepancy between simulated and observed data is an overestimate of simulated AAIW salinity, by up to 0.2. This is confirmed by the vertical profile of salinity differences (observed-simulated) as the median of all differences deviates from 0 at 800 m depth (Figure 3c). There are also biases of salinity in the upper ocean, near 250 m depth (within STSW, where the model tends to underestimate salinity) and below the surface (where the model is too salty). The salinity bias at 800 m depth seems to be associated with a warm temperature bias,

Figure 3. Validation of simulated temperature and salinity in the SWIO: probability density function (colors, in logarithmic scale) and median (thick black line) of the (b) temperature and (c) salinity biases merged over 2003–2009 between observed ARGO profiles and collocated model outputs (profile stations located by blue dots in Figure 3a); time series of (d) SST and (e) SSS in model (red) and (a) observations (black), within the red box. SST observations are from TMI data set while SSS observations are deduced from ARGO profiles.

Figure 4. Temperature-salinity diagram from Argo float measurements (black points) and colocated (in space and time) MARS model outputs (red points), and from MARS simulation at location of mooring 63 (solid cyan line) and 27 (dashed green line) of *New et al.* [2007, Figure 8a]. The solid black lines indicate σ_0 isopycnals (labeled in kg/m^3).

although the latter is maximum at 900 m depth (Figure 3b), which was not obvious in the temperature-salinity diagram (Figure 4). The overestimated salinity of AAIW and the underestimated salinity of STSW suggest that diapycnal mixing could be excessive due to the misalignment of the diffusion operator stencil with the isopycnals in a sigma-coordinate model [*Marchesiello et al.*, 2009]. The other salinity biases are not systematically related to temperature biases: the simulated outputs tend to be cooler than observations from the subsurface down to 750 m depth, with a maximum at about 250 m depth.

New et al. [2007] used observations taken during RSS Charles Darwin Cruise 141 to contrast the T/S structure to the east and to the west of the Mascarene Ridge, in order to highlight a likely impact of this topographic feature on surrounding water masses. Simulated outputs were extracted at the same location and averaged over the same time period (from 1 June to 11 July 2002). The T/S profile to the west of the Mascarene Ridge (station 63, solid cyan line in Figure 4) shows less contrasts among water masses, in particular in salinity, compared to the east of the Ridge (station 27, dashed green line). This is consistent with observations of *New et al.* [2007] (their Figure 8a), and suggests that the presence of topography enhances mixing among water masses (the predominant mean flow being oriented westward over the ridge).

Finally, sea surface temperature and salinity are compared with, respectively, TMI and ARGO observations, to the northwest of RI and MI (within the red box of Figure 3a). The simulated SST compares with observations for the mean, the seasonal fluctuations, the interannual variability as well as the occurrence of subannual events such as Cyclone Gamede which induced a sharp decrease of 4.5°C in early 2007 (Figure 3d). The validation of simulated SSS fluctuations is more difficult to perform due to the lack of observations (here we use salinity from ARGO linearly interpolated at 10 m depth). Still, there are some similarities between simulated and observed data, such as the decline in SSS in the first half of 2008 (Figure 3e).
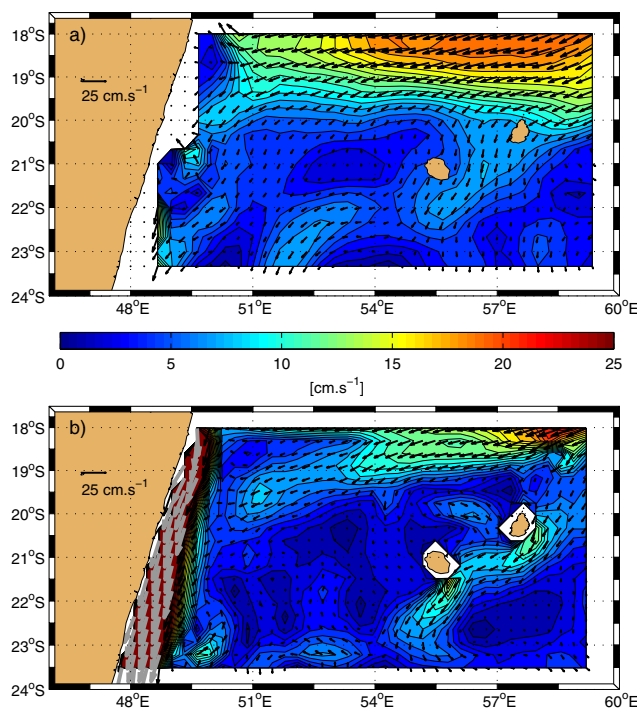
4. Upper Ocean Circulation

The observed mean circulation in SWIO, as described by OSCAR, is characterized by an intense westward circulation in the northern part of the region (with currents up to 20 cm s^{-1}) and southwestward currents around both sides of MI and to the east and south of RI (Figure 5a). The latter are notably weaker, reaching a maximum of 10 cm s^{-1} to the east of RI. Currents are even weaker in the southeast corner of the domain, and to the west of RI. Note that this data set does not reproduce the southwestward flowing SEMC, because of inaccuracy of the satellite observations near the coast of Madagascar and insufficient horizontal resolution.

The simulated mean circulation (Figure 5b) has similar large-scale characteristics, with westward currents to the north of the region and southwestward currents near the islands. Nevertheless, the high resolution of the model allows a better resolution of the circulation around the islands, which notably differs from the previous picture (Figure 5a). The predominant southwestward flow is only visible to the southeast of RI and MI, and is locally maximum at the offshore of each island, with currents faster than 12 cm s^{-1} (and up to 15 cm s^{-1} near RI). Between the two islands, the mean currents are oriented eastward north of RI and south-eastward to the west of MI, forming a recirculation from the northwest of RI to the western shore of MI. This recirculation, which is not present in observed data set, is presumably associated with the fact that the westward flow to the north of the region does not penetrate as far south in the model as observed. The
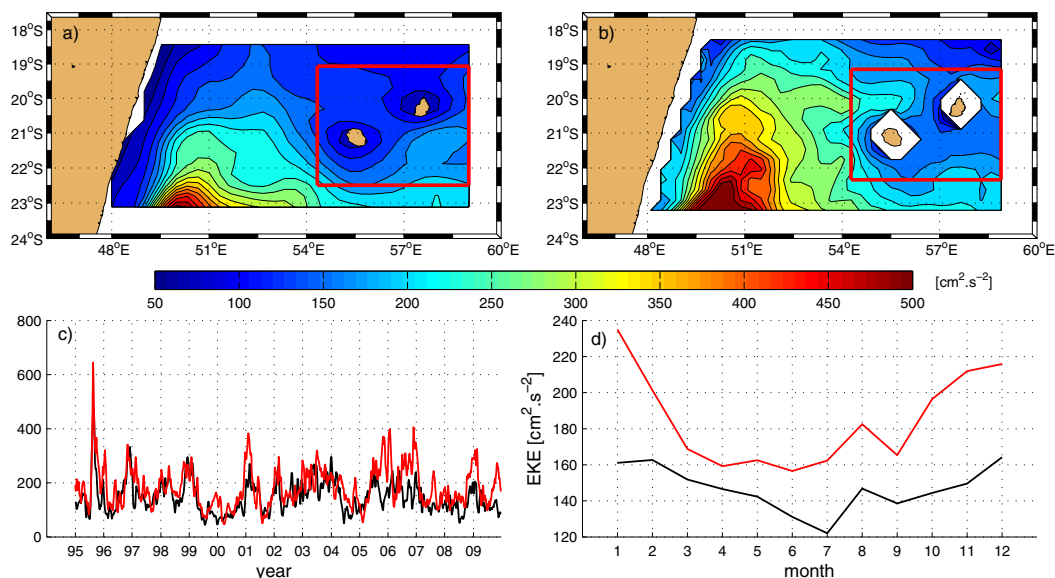
Figure 5. Upper ocean currents (at 15 m depth) averaged from 1994 to 2009 (a) in observations (OSCAR data set) and (b) in the simulation (only 1 vector every 16 is shown). Color shading indicates the magnitude of the currents (currents of amplitude larger than 25 cm s^{-1} are rescaled to fixed length and shown in gray), black lines are drawn every 1 cm s^{-1}.

latter may also be affected by the northern boundary of the model configuration (located at 18°S). As found in observations, the simulated circulation is the weakest in the southeast corner of the domain and to the west of RI. In the model, SEMC speed is of the order of 50–100 cm s^{-1}, consistent with in situ direct observations [*Schott et al.*, 1988].
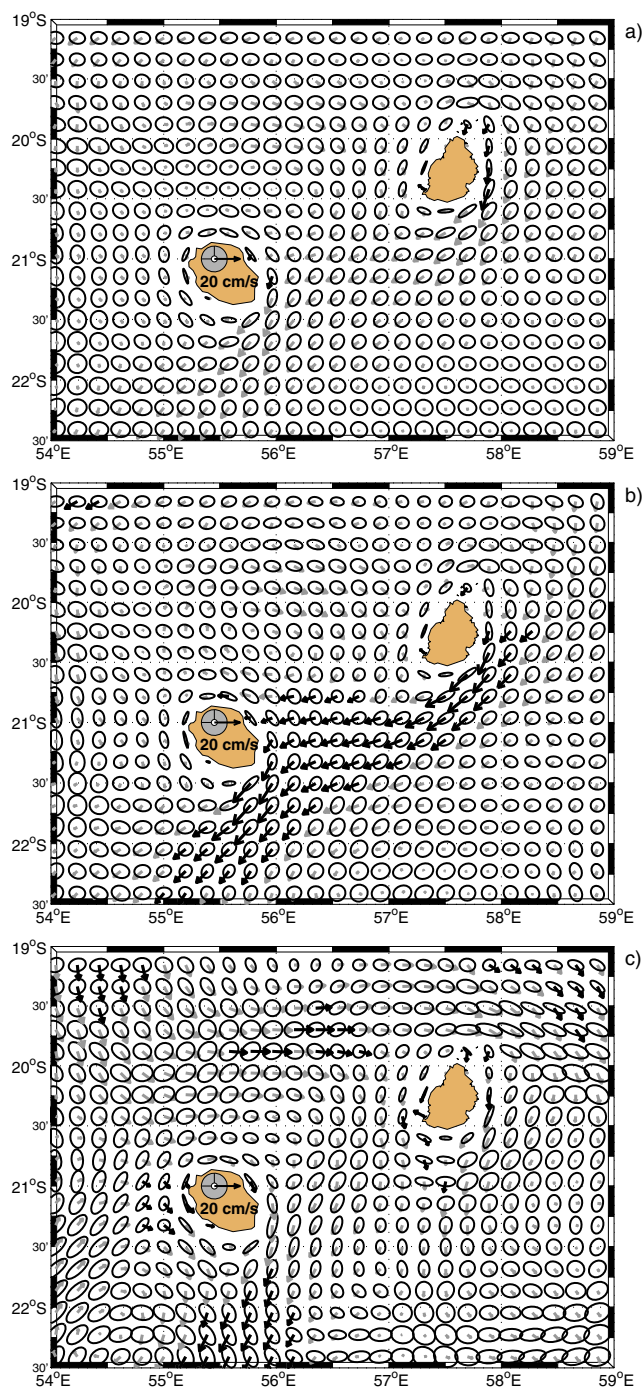
Variability of the upper ocean currents, as illustrated by EKE deduced from AVISO SSH, is maximum (up to 500 cm^2 s^{-2}) to the southwest of RI (Figure 6a), which is presumably associated with changes in intensity and/or position of the SICC [*Palastanga et al.*, 2007]. It is much smaller, of the order of 50–100 cm^2 s^{-2}, in the northern part of the domain, around the islands and along Madagascar eastern shore (for the same reasons as mentioned above for the mean SEMC). Simulated EKE (calculated from SSH as for observations) is generally larger than observed, and the maximum to the southwest of RI penetrates further north and extends to the north of RI (Figure 6b). Although this is visible in other model experiments [*Quartly et al.*, 2006], it may also be due to incompatibilities between the regional model circulation and conditions imposed along the open southern boundary of the configuration. Note that simulated EKE here uses MARS-dec outputs to match with the horizontal resolution of AVISO, to

Figure 6. Eddy Kinetic Energy in the SWIO: estimated (a) in observations and (b) in the simulation, calculated from surface geostrophic currents (in the model, currents were first decimated to fit the horizontal resolution of observations) and averaged over the period 1994–2009; (c) weekly EKE averaged over the red box (with observations in black and simulation in red) and (d) monthly mean climatology of those time series.
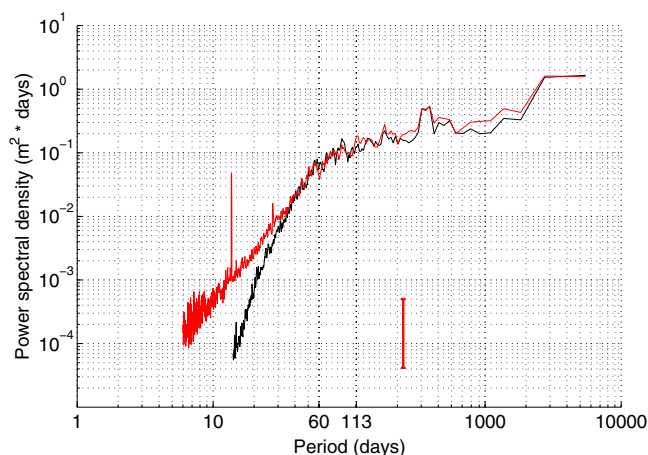
Figure 7. Upper ocean circulation (at 15 m depth) in the vicinity of La Réunion and Mauritius islands: mean currents (gray arrows) and standard deviation (ellipses) based on monthly averages for the period 1994–2009, (a) over all months, (b) August-September-October, and (c) January. Currents whose mean amplitude exceeds the standard deviation (in the direction of the mean current) are shown in black. Note that current speed and standard deviation use different scales (see inlet over RI). Only 1 vector and ellipse every 10 grid points is drawn.

ensure that the comparison is robust. The overestimation of EKE in the model, when averaged in the surroundings of the islands (Figure 6b, red box), amounts to 25% of the observed value. In this region, the observed and simulated time series show similar interannual fluctuations (Figure 6c), but it is beyond the scope of this paper to investigate those in details. We still note that the years of maximum EKE do not correspond to those described in *Jia et al.* [2011], who integrated EKE over the Indian Ocean to the east of our region (60–120°E). EKE in the vicinity of RI and MI also exhibits seasonal fluctuations, as shown by the monthly climatology: it is maximum in austral summer and minimum in winter (Figure 6d). It is well reproduced by the model, although the standard deviation of the monthly climatology is twice as large as that observed. This seasonal cycle is similar to the seasonal changes of EKE along 25°S noted by *Palastanga et al.* [2007] and over the southeast Indian Ocean noted by *Jia et al.* [2011]. The latter assessed that the seasonal modulation of EKE is mediated by baroclinic instability associated with the surface-intensified SICC and the underlying SEC system. A similar seasonal modulation of EKE has been observed in the subtropical Pacific, and attributed to seasonality of the baroclinic instability of the background mean circulation [*Qiu*, 1999; *Qiu and Chen*, 2004, 2010].

We now focus on the simulated circulation in the vicinity of RI and MI (satellite observations are inaccurate near the coasts and have insufficient horizontal resolution to reproduce this). The direction of the mean currents has already been described above (using Figure 5). Figure 7 shows, in addition, the ellipse of variability of the currents and highlights those whose mean amplitude is larger than the standard deviation in the direction of the mean current (black arrows). In the following, we designate such currents, which temporal mean amplitude is likely to be seen most of the time, as significant. For the temporal mean over all months, there are only few significant currents,

Figure 8. Power spectral density of SLA from AVISO (black line) and from MARS model outputs (red line) over the 1994–2009 period. Spectra are calculated (on all AVISO grid points and on 1 every 10 model grid points) using multitaper method using three windows, then averaged over the SWIO (18–23°S; 50–59°E). Red vertical bar shows the 95% uncertainty level.

very close to RI and MI (Figure 7a). Hence, most of the vicinity of the islands is dominated by fluctuating currents, at least on the monthly time scale. In other words, the mean upper ocean circulation described above is not meaningful (except for the few isolated significant currents): it is very unlikely that any snapshot of the circulation in the vicinity of the islands follows this description. The southwestward circulation to the southeast of the islands is significant in August-September-October only (Figure 7b). It is associated with an intense westward current to the east of RI. The recirculation to the north of RI, although visi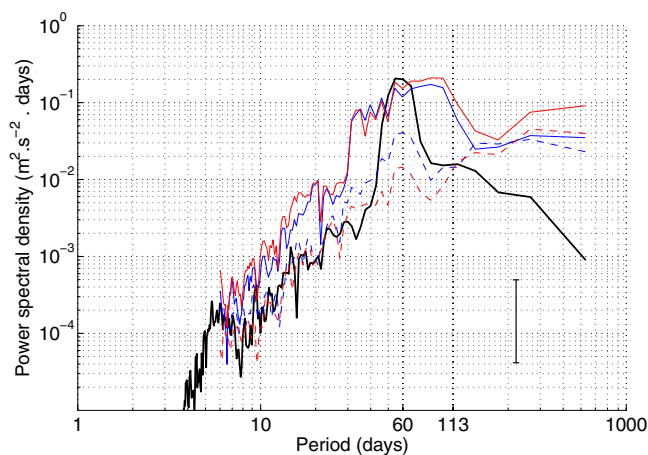ble on the overall mean and almost every month, is only significant in January (Figure 7c). In fact, the circulation around RI and MI is dominated by transient features, which are described, illustrated and investigated below.

5. Mesoscale Processes in the Vicinity of the Islands

Transient features in the circulation around RI and MI project directly onto SLA whose power spectrum has no significant peak but a sharp change of slope at 60 day period (Figure 8). Observed (black line) and simulated (red line) power spectra are very similar for periods longer than 40 days. At higher frequency, two peaks are visible in the model spectrum at 28 day and 14 day periods, although the former is not significant, which are not visible in the observed spectrum. They are likely related to tidal constituents M_f and M_m that were not removed by the Demerliac filter (but that were removed by tidal filtering of AVISO MADT). *Cordier et al.* [2013] have shown that these long-period tidal constituents contribute significantly to the sea level variations in RI. Also, the level of power spectrum density for periods 14–40 days is higher in the model compared to observations, which may be due to the contribution of processes at small spatial scale not observed by AVISO. The change of slope at 60 day period suggests that this is a predominant time scale of variability for both the observed and simulated SLA in the SWIO. Such an interpretation of a change of slope in power spectrum can be drawn analytically for a first-order autoregressive process (aka Markov Process): the change of slope occurs at the damping time scale—but it is valid for any type of process. This time scale is the most visible when looking at the time series. Note that it differs in nature from periodic time scales, for which power spectrum would peak.

Direct observations of the circulation at depth to the east of Madagascar (ICM3 records, part of WOCE project) revealed a peak of variability at 60 day period in the power spectral density of meridional velocity, as illustrated by *Warren et al.* [2002, Figure 3, mooring 6a, reproduced in Figure 9 in black]. These authors suggest that it reflects a barotropic mode of variability (they lack measurements in the upper ocean to verify this directly), which is confirmed by the theoretical model of *Weijer* [2008]. This mode is a free mode of oscillation of an ocean at rest; it features westward propagation of anomalies that are elongated in the meridional direction, albeit with a tilt of about 19° from due north, imposed by the slanted coastline of Madagascar [*Weijer*, 2008]. Power spectral analysis of the model meridional velocity in the vicinity of the mooring location at 2500 m depth (and for the same time period as observations, from 1995 to 1997) shows enhanced variance around 60 day period (Figure 9, red solid line), consistent with the observations although the peak is much broader in the model. Also, in the model spectra, this peak superimposes on a change of slope that is very similar to that observed for MADT. We confirm that it reflects a barotropic mode of variability, as the power spectral density of the barotropic meridional velocity at that location is almost superimposed (blue solid line). Hence, our model reproduces the barotropic Rossby basin mode of the Mascarene Basin, as

Figure 9. Power spectral density of meridional velocity at 2500 m depth in observations (black) and model (red, solid line) near mooring 6a (20°S, 52.52°E) [*Warren et al.*, 2002], and of the barotropic velocity in the model (blue, solid line) at the same location. Dashed lines reflect similar analysis of the model outputs to the east of MI (20°S, 58.7°E, meridional velocity at 2500 m depth, dashed red and barotropic velocity, dashed blue). This analysis was performed over the period 1995–1997 when observations were available. Spectra are calculated using multitaper method with three windows. Vertical bar shows the 95% uncertainty level.

defined by *Weijer* [2008]. We verify that this mode is not visible to the east of MI: the change of slope at 60 day is visible but the peak related to the barotropic mode is not significant (dashed lines). It remains to explain the change of slope at 60 day, visible in SLA power spectra, meridional and zonal (not shown) velocities, nearly everywhere in the SWIO. To better understand why this is a predominant time scale of variability, we develop two approaches in the following: (i) an Eulerian perspective that highlights westward propagating anomalies and (ii) a Lagrangian perspective that identifies individual eddies in the SWIO.

5.1. Westward Propagating Anomalies

As found in previous studies [*Morrow and Birol*, 1998; *Schouten et al.*, 2002a; *Quartly et al.*, 2006; *Palastanga et al.*, 2007], anomalies in sea surface height mostly propagate westward in the SWIO, hence we only show the westward filtered anomalies at 21°S (see *Cipollini et al.* [2001], for details on the method, which also filters out the variability at 1 cpy) (Figures 10a and 10b). Over the period 1994–2009, there are approximately 4.9 structures in observations and 5.2 structures in the model, that propagate every year across the SWIO (this has been quantified by measuring the occurrences of changes in the sign of anomalies at fixed longitudes). This average number of events is roughly consistent with the 60 day predominant time scale of the SLA spectra. Note that the observed (Figure 10a) and simulated (Figure 10b) Hovmöller diagrams render similar frequencies of westward propagating anomalies in spite of the fact that individual events do not exactly match each other in observations and model outputs. Model outputs also reveal that the westward propagation of anomalies is not systematically influenced by the presence of RI.

The propagation speed of the westward propagating anomalies, estimated using a Radon method [*Challenor et al.*, 2001], is approximately 8 cm s^{-1} (respectively, 9.3 cm s^{-1}) in the simulation (observations) at 21°S (Figure 10c, observation in black and model in red). Indeed, propagation speed of 8 cm s^{-1} overlaid on the Hovmöller diagrams (Figures 10a and 10b) matches well the westward propagation of SLA. Figure 10c shows that the propagation speed increases as latitude decreases, from 6–7 cm s^{-1} at 23.5°S to 11–12 cm s^{-1} at 18.5°S, both in the model and the observations, although the model slightly underestimates the propagation speed, by up to 1.3 cm s^{-1} at 21°S. To the north of 19°S, the westward propagation speed decreases notably, which may reflect limitations of the use of the Radon method in a relatively small domain.
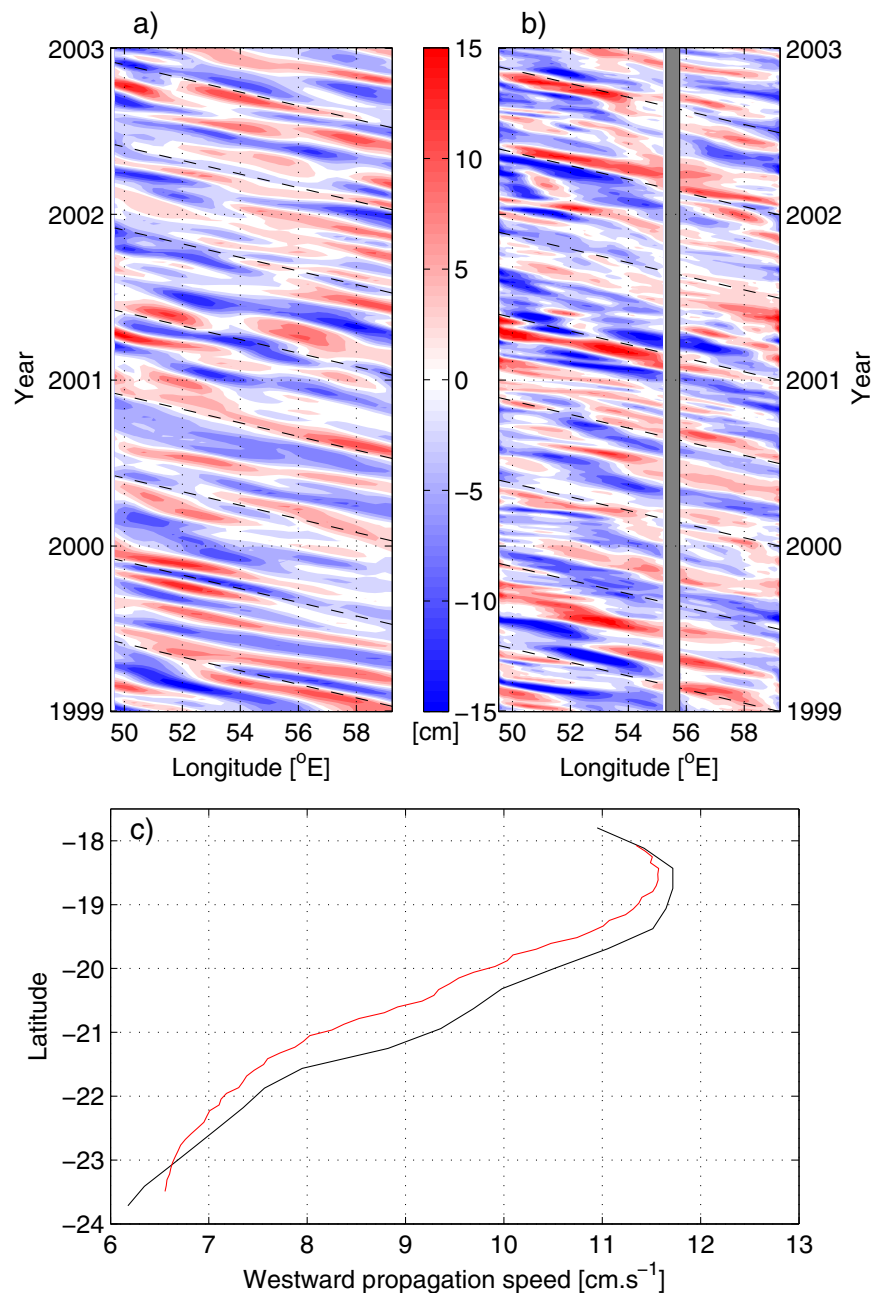
The spatial scale of these westward propagating anomalies is estimated using wave number-spectra of SLA at 21°S and between 49°E and 60°E over the period 1994–2009. A sharp change of slope occurs at a wavelength of around 400 km both in observations and simulated outputs (not shown). This is consistent with *Palastanga et al.* [2007] who estimated the wavelength of those anomalies to be 440 km, using the same observed data set at 25°S and between 50°E and 110°E over the period 1992–2004.

These westward propagating anomalies have been related to incoming Rossby waves that cross the Indian Ocean [*Palastanga et al.*, 2007], but this remains unclear. The first baroclinic Rossby radius of deformation obtained by solving a Sturm-Liouville eigenvalue problem [*Chelton et al.*, 1998; *Killworth et al.*, 1997] on the mean density profile derived from the model outputs) near RI is $R \sim 56$ km at 21°S. The wavelength associated with the first baroclinic Rossby waves is $2\pi R \sim 352$ km [e.g., *Pedlosky*, 1987; *Lin et al.*, 2014], which is comparable to the wavelength that we estimated in the SWIO. A paradigm occurs when we compare our

Figure 10. Hovmöller diagram of SLA along 21°S (a) in AVISO observations and (b) MARS outputs. Anomalies are westward filtered (using a spatial Fourier transform) and the seasonal variability has been removed. Dashed lines indicate propagation speed of 8 cm s⁻¹. (c) The estimated westward propagation speed (calculated using a Radon transform) as a function of latitude, in observations (black) and model (red).

estimate for the period and westward propagation speed with what is expected from theoretical arguments. In a resting ocean and in the long-wave limit, the dominant first baroclinic mode has a westward phase speed given by $-\beta R^2$, where β is the Coriolis parameter. At 21°S, this yields a phase speed of 6.7 cm s⁻¹, as found in previous studies [*Chelton et al.*, 2007, 2011], which is consistent with our estimate of the propagation speed for anomalies in the SWIO. Yet this linear theory is a crude simplification of the Rossby waves dynamics. Following the full dispersion relation for Rossby waves in the zonal direction: $\omega = -\beta k(k^2 + R^{-2})^{-1}$, where k is the zonal wave number, and assuming a wavelength of 400 km, the period of those waves is expected to be ~122 days and the phase speed ~3.8 cm s⁻¹, as found in *Warren et al.* [2002]. This does not match our estimates of westward propagation speed nor the 60 day predominant

time scale of power spectral density. Hence, it is not straightforward to relate the 60 day predominant time scale of variability in the SWIO to baroclinic Rossby waves crossing the Indian Ocean. Indeed, RI and MI stand near the critical latitude where mesoscale features are nonlinear [*Chelton et al.*, 2011].

5.2. Eddies

There is uncertainty in the interpretation of Hovmöller diagrams as propagating waves, as series of eddies propagating in the same direction (here westward) may leave the same imprint in SLA [*Quartly et al.*, 2006]. In the following, we assume that these anomalies are due to propagating eddies and apply an eddy-tracking method to determine their characteristics, in AVISO, MARS-dec, and MARS data sets. Note that MARS-dec outputs were smoothed by a moving average over 3×3 points, to ensure spatial coherence between the structures. Figure 11 shows the positions and trajectories of anticyclonic and cyclonic eddies tracked in the box 47–59.3°E, 18–23.5°S over a 16 years period (1994–2009). Table 1 summarizes the basic eddy properties such as the number of eddies tracked, their mean life-time (time span when each individual eddy was detected), amplitude (maximum SSH), and size (radius).
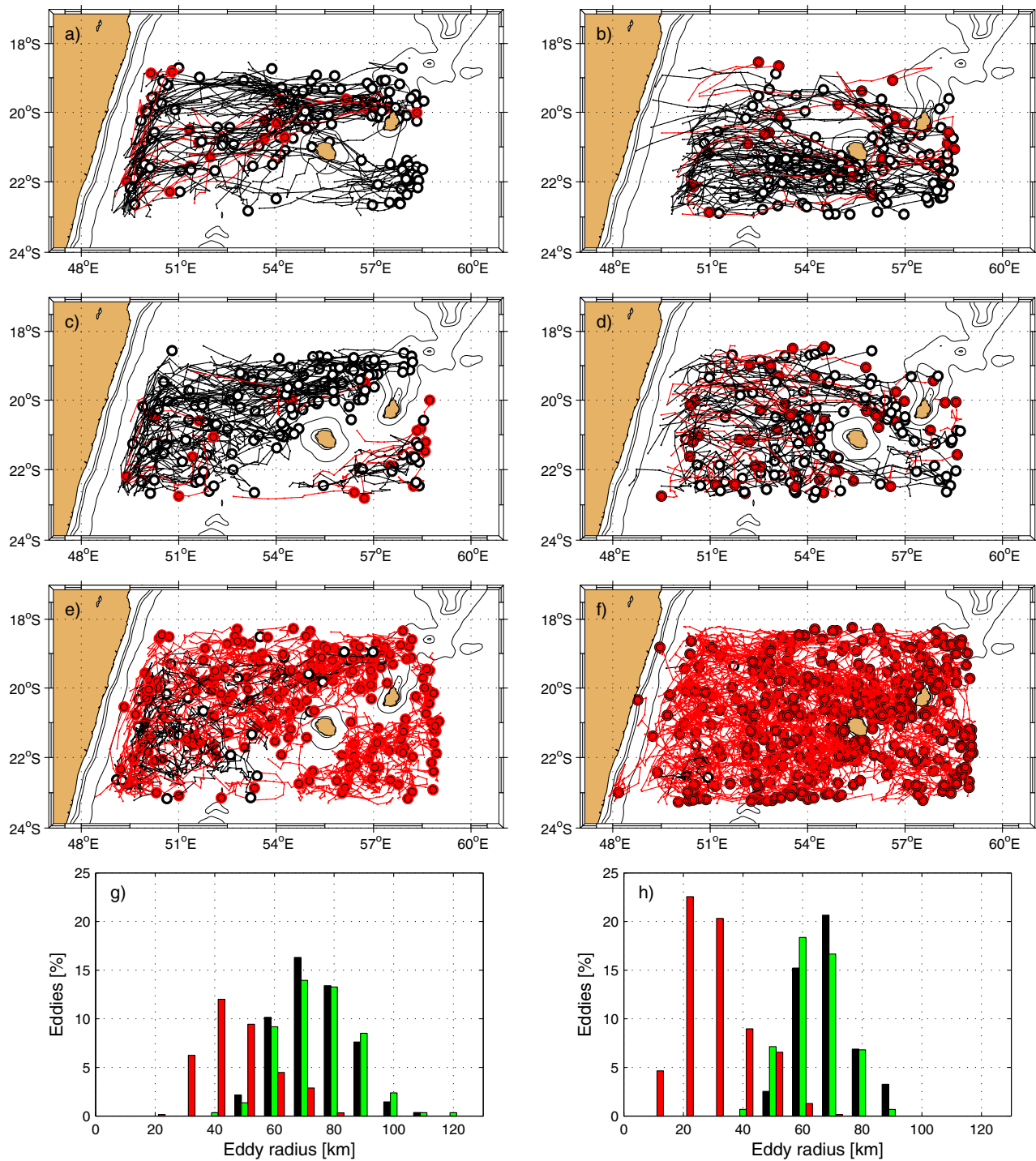
Tracking results obtained from AVISO and MARS-dec data sets are similar. Out of the 276 (respectively, 294) eddies tracked in AVISO (respectively, MARS-dec), 51.5% (respectively, 49.7%) were anticyclonic (Table 1). Associated SLA are small (5–6 cm for anticyclones-cyclones in both AVISO and MARS-dec, Table 1) compared to other regions (such as in the Mozambique Channel) [*Halo et al.*, 2014] and considering the accuracy of AVISO observations (of the order of 2 cm). Their distribution as a function of size is nearly symmetric, centered around 70–80 km for anticyclones and 60–70 km for cyclones (Figures 11g and 11h, black and green). Hence, cyclonic eddies are slightly smaller than anticyclonic eddies. Besides, there are more small cyclonic eddies than anticyclonic eddies (eddies with radius smaller than 60 km are indicated in red in Figures 11b and 11d), and those eddies tend to be more numerous in MARS-dec (Figure 11h).

The trajectories of tracked eddies are also similar in AVISO and MARS-dec. Eddies primarily propagate westward across the domain, with dissimilarities in the trajectory of anticyclones (Figure 11, left) and cyclones (Figure 11, right). Trajectories of anticyclones are visible everywhere in the domain, especially to the southwest of RI and MI (Figures 11a and 11c). This suggests that there are two main pathways for these eddies: to the north of the islands and to the south of the islands, with pathways slightly oriented southward. A third pathway is visible along the coast of Madagascar, oriented southward. Trajectories of cyclonic eddies, on the other hand, are visible everywhere in the domain but to the northwest of RI and MI (Figures 11b and 11d), and they are slightly oriented northward. A secondary pathway is also observed between RI and MI with a similar orientation. It is important to keep in mind that the islands are not visible in AVISO data set. Hence, it is even more surprising that the islands have such an imprint on the trajectories of eddies in this data set. The major difference between AVISO and MARS-dec trajectories can be seen for cyclones to the northwest of RI, where there are more small eddies in MARS-dec.

The discrepancy between anticyclones that tend to propagate southwestward, while cyclones tend to propagate northwestward, is confirmed by statistical analysis of their propagation speed in the meridional direction (selecting trajectories from 51°E to 59.3°E to exclude the southward trajectories along the coast of Madagascar). The ensemble average propagation speed for anticyclones is -0.32 cm s^{-1} in AVISO and -0.39 cm s^{-1} in MARS-dec, which are significantly different from 0 (using a Student's *t* test at 90% significant level). The ensemble average propagation speed for cyclones is 0.09 cm s^{-1} in AVISO and 0.60 cm s^{-1} in MARS-dec, but only the latter is significantly different from 0. These meridional tendencies in the trajectories of eddies, northward for cyclones and southward for anticyclones, is consistent with the results of *Morrow et al.* [2004] and *Chelton et al.* [2007, 2011]. We also note that cyclones are created and pass in between RI and MI, while there are very few anticyclones doing such.

Tracking results obtained for MARS data set (with no decimation) show a very contrasted situation. A larger number of eddies were tracked (625) compared to AVISO (276) and MARS-dec (294), 65% of which are cyclonic. The amplitude of the eddies is similar to those tracked in AVISO and MARS-dec, but their distribution as a function of size is significantly different (at 95% level using a chi-square test) from those in MARS-dec for both anticyclones and cyclones: in MARS, the mean size of anticyclones is 40–50 km and the mean size of cyclones is 20–30 km. Applying the tracking method on MARS identifies a much larger number of small eddies that significantly affects the mean size of eddies as well as their distribution as a function of sign, while those small eddies cannot be identified in AVISO nor MARS-dec. Note that the maximum size of

Figure 11. Tracks of eddies (anticyclones to the left, cyclones to the right) during the period 1994–2009 and their formation sites (black circles), (a and b) in AVISO, (c and d) in decimated MARS outputs (to mimic AVISO sampling, see text for details), and (e and f) in original MARS outputs. Eddies with a radius smaller than 60 km are shown in red. Only eddies with life duration larger than 30 days are shown on the map. Bottom panels show the eddy density distribution as a function of their radius, in AVISO (black bars), in decimated MARS outputs (green) and in original MARS outputs (red).

tracked eddies is also different in MARS and MARS-dec, suggesting that the tracking method applied in MARS-dec might conglomerate distinct eddies and, subsequently, overestimate their size. It is likely that the same is happening when tracking eddies in AVISO data set. The trajectories of eddies in MARS are similar to those described in MARS-dec and AVISO, except that there seems to be more eddies in the lee of RI and MI,

Table 1. Eddy Statistical Census 1994–2009 (1994–2000 for OBCCLIM Outputs)

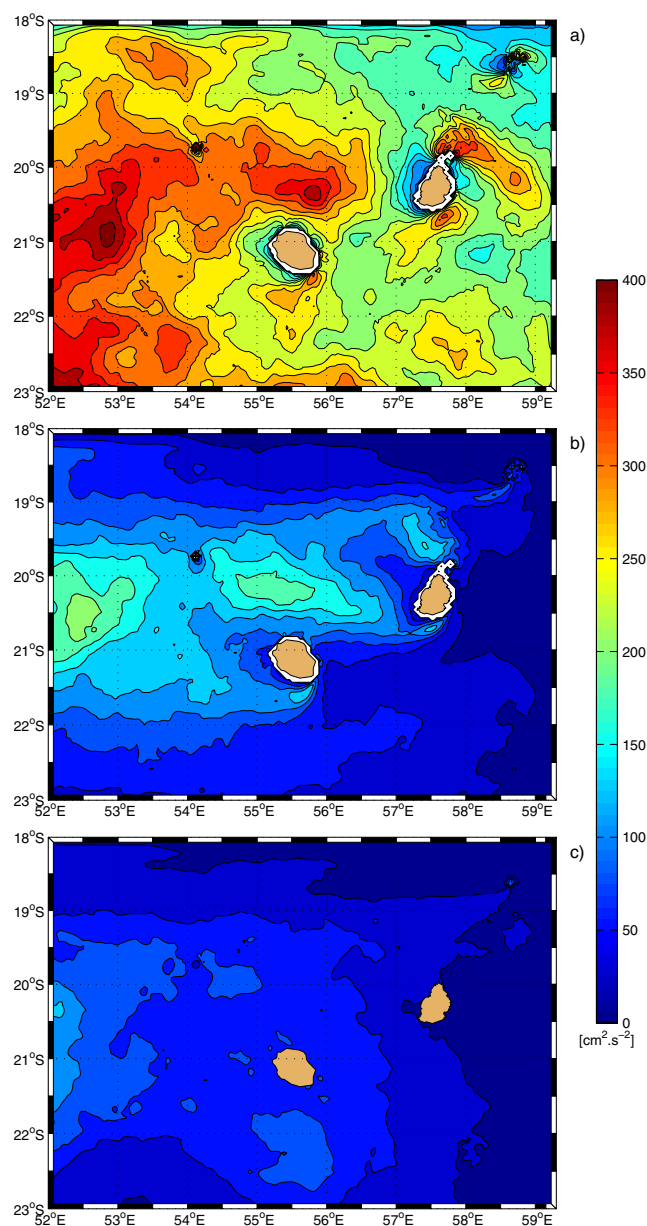|				Radius (km)
Eddy	Number of Eddies	Mean Life-Time (day)	Mean Amplitude (cm)	Min/Mean/Max
Altimetry				
Anticyclones	142	62	5	49/74/106
Cyclones	134	68	6	52/69/94
Model(MARS-dec)				
Anticyclones	146	57	5	45/75/117
Cyclones	148	56	6	43/64/95
Model(MARS)				
Anticyclones	222	49	6	18/46/78
Cyclones	403	52	6	11/30/70
Model(OBCCLIM)				
Anticyclones	86	49	3	20/36/59
Cyclones	255	58	3	8/22/54

which is discussed below. Finally, the mean life-time of eddies are shorter in MARS compared to AVISO and MARS-dec (Table 1). This is, presumably, a direct consequence of the difference in eddy sizes, as it has already been observed that small eddies have a relatively short life time while larger eddies live longer [*Chelton et al.*, 2011].

5.3. Origin of Mesoscale Processes

We compare the mean EKE in sensitivity experiments against the REF, the analogous of MARS on a smaller domain (Figure 12). Note that the picture of EKE in REF (Figure 12a) highlights a minimum in the close vicinity of the islands and local maxima to the north and to the south of RI and MI, which were not visible in the picture of EKE in MARS that was adapted to match AVISO sampling (Figure 6b). We quantify the contribution of the advection of mesoscale processes through the lateral open boundaries of the domain, and in particular through the eastern boundary. EKE in OBCCLIM (Figure 12b) is everywhere significantly much lower than in REF. The average of EKE over the whole domain reaches 75 cm^2 s^{-2} in OBCCLIM and 256 cm^2 s^{-2} in REF. Hence, approximately 70% of the mesoscale activity in REF (and, presumably in MARS) is associated with anomalies on the open boundaries of the domain, presumably the eastern boundary considering the predominant westward propagation illustrated above. It remains to be clarified whether the variability within the region reflects (i) the sole advection of anomalies from the eastern boundary or (ii) local instability processes (namely nonlinear interaction with topography) that are triggered by advected anomalies. EKE in experiment REF-NOISL has comparable amplitude to REF (253 cm^2 s^{-2}), although the patterns differ with maximum values to the south of 20°S (not shown). This suggests that most of the variability in the region is dominated by the advection of anomalies from the east, but those are significantly influenced by RI and MI.

EKE in OBCCLIM is maximum in the lee of the islands: to the south of RI and MI in the immediate vicinity of the islands, and then to the west of the islands, where it reaches half REF value. This suggests that mesoscale processes are generated locally, presumably due to the interaction between the background mean flow, oriented southwestward, and the islands. A symmetric pattern of enhanced EKE is also found to the north of MI. Tracking the eddies in OBCCLIM shows that this patch of EKE is primarily related to cyclonic eddies (75% of all eddies in OBCCLIM are cyclones), whose amplitude (3 cm) and size (21 km) are smaller than cyclones tracked in MARS (Table 1). This mechanism of local generation is confirmed by OBCCLIM-NOISL (Figure 12c), in which the bathymetry has been flattened in place of RI and MI, and which does not show an EKE enhancement in the lee of the islands. Note that EKE present a small maximum along the western boundary of the domain because the open-boundary algorithm prevents some mesoscale features from leaving the domain to the west. EKE in OBCCLIM-NOISL is also slightly enhanced to the lee of 58.7°E; 18.6°S, and 54.15°E; 19.7°S, where bathymetric shallows are present.

In OBCCLIM-NOISL, EKE averaged over the whole domain is only 46 cm^2 s^{-2}, roughly 18% of the REF value, reflecting the contribution of local atmospheric forcing to mesoscale processes (with no interaction with the islands). To quantify the direct role of wind forcing in the local generation of mesoscale processes, we additionally ran experiment NOWIND where there is no wind stress (but the wind module still contributes to the calculation of air sea heat fluxes via the bulk formula). Away from the western boundary (where
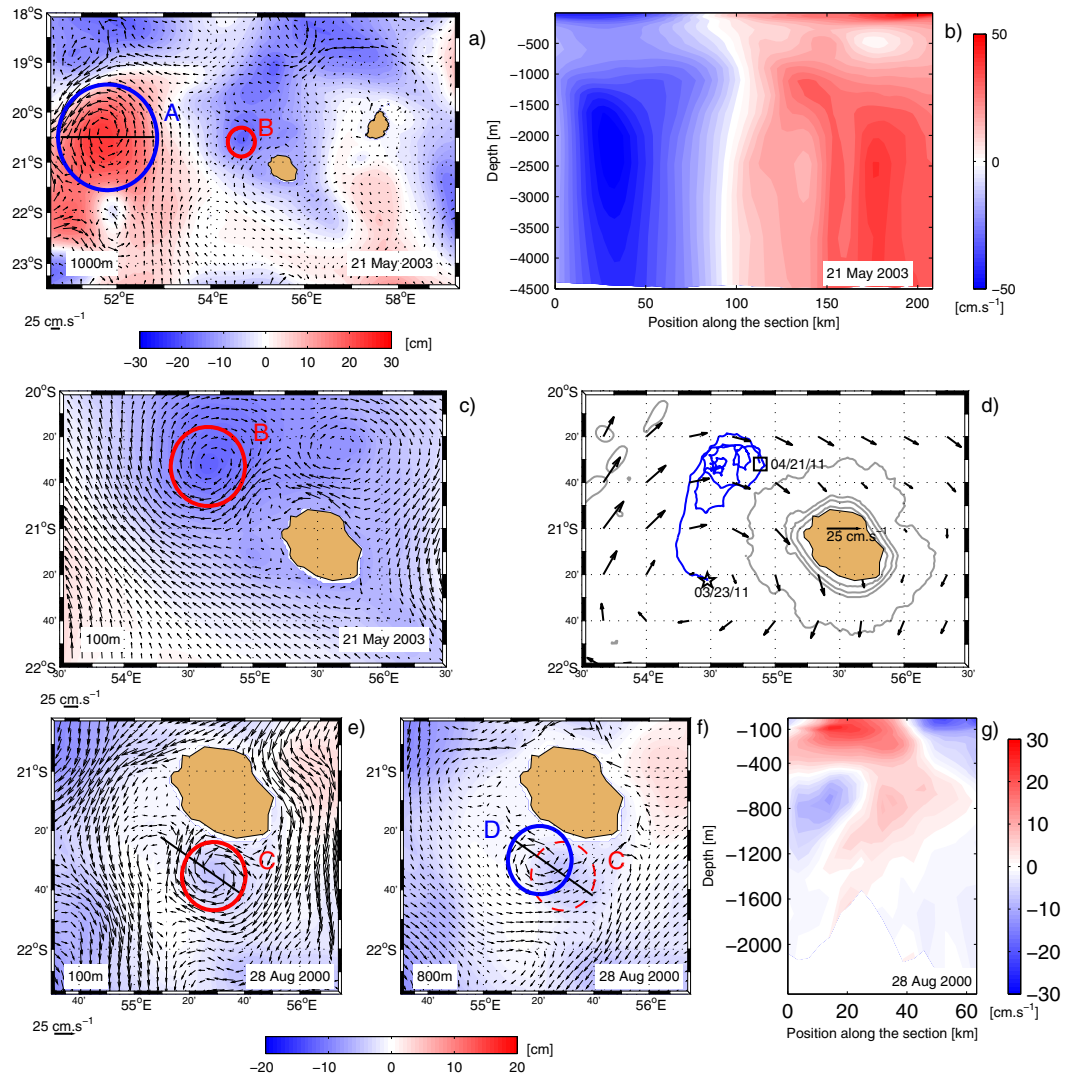
Figure 12. Mean EKE over 1994–2000 for (a) REF (full forcings), (b) OBCCLIM (climatological open-boundary condition), and (c) OBCCLIM-NOISL (with an idealized version of the bathymetry that does not reproduce RI and MI). Only one in every two grid points is used for this diagnosis.

inconsistencies between atmospheric forcing and the open-boundary conditions enhances turbulence), EKE in NOWIND is very similar to REF, which suggests that wind forcing has little direct impact on the local generation of mesoscale processes. Note that the wind stress data set used to force all experiments does not resolve RI and MI, i.e., does not reproduce the wind wakes of the islands that are expected to affect the upper ocean dynamics [*Dong et al.*, 2007]. In experiment WRF, we used a dynamical downscaling of the wind data set to introduce the wind wake, and compared twin simulations with and without islands in the atmospheric model. The resulting anomalies in EKE are positive to the south of RI, but of relatively small amplitude (less than 100 cm^2 s^{-2}) and very patchy everywhere else in the domain (not shown). The fact they are of comparable magnitude as the background EKE as given by OBCCLIM-NOISL, suggests that they reflect a change in the mean circulation rather than the local enhancement of mesoscale processes in the lee of RI.

5.4. Vertical Structure

It is a challenging matter to characterize the vertical structure of mesoscale processes in MARS, due to a large variety present in the system. Rather, we illustrate a few examples that have markedly different structures (Figure 13). In Figure 13a, the Anticyclone A was visible in May 2003 to the west of

RI, close to the location of mooring 6a of *Warren et al.* [2002]. It is clearly barotropic (Figure 13b), although with a small decrease in meridional velocity at about 500 m depth. This is consistent with observations of barotropic meridional velocity anomalies at mooring 6a [*Warren et al.*, 2002]. On the contrary, cyclone B (Figure 13c) that was visible at the same period but closer to RI is baroclinic: cyclonic velocities are hardly visible at 1000 m depth (Figure 13a). Note that neither of these two eddies is associated with a round-shaped SLA pattern, although anticyclone A is found in a region of positive SLA while cyclone is merged in a region of negative SLA. On the other hand, cyclone C (Figure 13e) that was generated to the south of RI in August 2000 is clearly associated with negative round-shaped SLA. Its vertical structure is of yet another type: velocities contributing to the cyclonic motion only extend down to 500 m, and change sign below, suggesting that the cyclone C is linked to an anticyclone, noted D, below (Figures 13f and 13g).

Figure 13. Illustrations of the vertical structure of individual eddies: (a) snapshot of SLA (shading) and circulation at 1000 m depth (arrows) on 21 May 2003 that shows anticyclone A and cyclone B, (b) meridional current within anticyclone A, (c) zoom on cyclone B with SLA (shading) and circulation at 100 m depth (arrows), (d) trajectory of drifter No. 102032 overlaid on OSCAR currents during the corresponding period, (e) snapshot of SLA (shading) and circulation at 100 m depth (arrows) on 28 Aug 2000 that shows cyclone C, (f) circulation at 800 m depth, showing cyclone C and anticyclone D, and (g) meridional current along black section in Figures 13e and 13f.

We finally consider more closely the trajectory of drifter No. 102032 from 23 March to 21 April 2011 (Figure 13d). After a northward drift of about 120 km (at up to 70 cm s^{-1}), the drifter described circular clockwise motion (at 20–30 cm s^{-1}) within 30–50 km to the northwest of RI. Meanwhile, the large-scale surface circulation, as given by OSCAR, was relatively steady, describing a cyclonic motion of much larger spatial scale. Hence, where the buoy drifted northward, it followed the direction of OSCAR currents. Later, while the buoy drifted in a circular motion, the OSCAR currents were oriented to the east-southeast. Obviously, this part of the drifter trajectory reflects surface currents that were not captured by OSCAR. Such currents may have been associated to a cyclone similar to cyclone B, which somehow supports the realism of mesoscale processes produced by MARS. Overall, this highlights the limitation of low-resolution circulation products like OSCAR, to describe efficiently the synoptic circulation in this region.

6. Summary and Discussion

In this study, we document the circulation in the vicinity of La Réunion and Mauritius islands (RI and MI). Because direct observations are sparse, we developed a modeling strategy to reproduce, in

POUS ET AL. 1973

a more realistic way, the circulation from January 1994 to December 2009. We first validated MARS outputs against available observations: SLA observed by satellite and at a tide-gauge station and temperature and salinity from ARGO floats and interpolated products. Although the model has some biases in temperature and salinity at depth, SLA and water mass properties are satisfactorily reproduced.

MARS large-scale circulation in the SWIO compares with observations. Nevertheless, the high resolution of the model allows to resolve the circulation around RI and MI and reveals locally maximal circulation, oriented southwestward, to the southeast of each island. There also exists a recirculation from the northwest of RI to the western shore of MI, not visible in the observed data set. Yet variability of the upper ocean is so large that the temporal mean circulation does not depict well the synoptic circulation, which is dominated by westward propagating features.

Power spectrum density of SLA in MARS compares favorably with observations, and both exhibit a predominant time scale of 60 day. This time scale coincides with the period of a barotropic mode of variability in the Mascarene Basin, hypothesized by *Warren et al.* [2002] and *Weijer* [2008], but this mechanism does not suffice to explain the predominant 60 day period of SLA as it is limited to the west of RI and MI while SLA propagating westward are visible to the east of the islands. Investigating SLA in a Eulerian perspective, we characterize their frequency of occurrence (approximately five each year), their propagation speed (of the order of 8 cm s^{-1} at the latitude of RI) and spatial scale (400 km). It is not straightforward to relate these characteristics to baroclinic Rossby waves crossing the Indian Ocean. Although the wavelength matches the first baroclinic Rossby radius of deformation, the propagation speed in MARS is only consistent with the first baroclinic mode westward phase speed in the long-wave resting ocean limit, an admittedly crude simplification of Rossby wave dynamics. Besides, RI and MI stand near the critical latitude where mesoscale features are nonlinear [*Chelton et al.*, 2011].

Tracking those westward propagating features as eddies, we gain a more detailed understanding of the dynamics in this region. First, we emphasize how the low-resolution sampling of AVISO affects the characteristics of mesoscale eddies. Then, we confirm that eddies have a meridional tendency in their trajectory, northward for cyclones and southward for anticyclones, which is consistent with the results of *Morrow et al.* [2004] and *Chelton et al.* [2007, 2011]. By running sensitivity experiments on the boundary conditions, we propose the origin of those mesoscale processes. While the majority of mesoscale processes are advected through the boundaries of the domain, eddies are also generated locally in the region. The mean southwestward circulation that encounters RI and MI, as well as eddies advected from the east, interact with the topography and this generates smaller eddies that drift to the west of the islands. Those eddies are predominantly cyclones rather than anticyclones, which may be due to the centrifugal instability of anticylonic eddies [*Dong and McWilliams*, 2007], although other mechanisms may also be at play. We have noted that wind forcing does not contribute to the local generation of mesoscale processes in the domain. Overall, it remains unclear whether and how these mesoscale processes induce a predominant time scale of 60 day in SLA. Also, one has to keep in mind the limits of eddy-tracking methods in the presence of islands (eddies may artificially split or merge as they propagate around an island).

Observations and our simulation show that there is interannual variability in the mesoscale processes, which is not specifically investigated here. It has been shown by *Palastanga et al.* [2006] that this variability is related to the arrival of large-scale anomalies that propagate westward along 10–15°S in response to the Indian Ocean dipole (IOD) events.

As a conclusion, the circulation in the vicinity of RI and MI reflects the high degree of complexity of ocean dynamics in this region, influenced by regional ocean modes of variability, as well as remotely generated mesoscale processes that are advected from the east. MARS produces a large variety of eddies in the region, which dominate the circulation in the vicinity of the islands. These mesoscale processes cannot be directly validated because satellite observations lack horizontal resolution. Still, they are in agreement with the trajectory of three buoys that drifted in the vicinity of RI. This advocates for more direct observations of the mesoscale processes in the SWIO, as they are likely to contribute the most to the ocean impact on marine ecosystems.

References

Becker, J. J., et al. (2009), Global bathymetry and elevation data at 30 arc seconds resolution: SRTM30_PLUS, *Mar. Geod.*, *32*(4), 355–371, doi:10.1080/01490410903297766.

Birol, F., and R. Morrow (2001), Source of the baroclinic waves in the southeast Indian Ocean, *J. Geophys. Res.*, *106*, 9145–9160.

Birol, F., and R. Morrow (2003), Separation of quasi-semiannual Rossby waves from the eastern boundary of the Indian Ocean, *J. Mar. Res.*, *61*(6), 707–723.

Bonjean, F., and G. S. E. Lagerloef (2002), Diagnostic model and analysis of the surface currents in the tropical Pacific Ocean, *J. Phys. Oceanogr.*, *32*(10), 2938–2954, doi:10.1175/1520-0485(2002)032¡2938:DMAAOT¿2.0.CO;2.

Challenor, P. G., P. Cipollini, and D. Cromwell (2001), Use of the 3D Radon transform to examine the properties of oceanic Rossby waves, *J. Atmos. Oceanic Technol.*, *18*, 1558–1566.

Chelton, D., R. Deszoeke, M. G. Schlax, K. El Naggar, and N. Siwertz (1998), Geographical variability of the first baroclinic Rossby radius of deformation, *J. Phys. Oceanogr.*, *28*(3), 433–460.

Chelton, D. B., M. G. Schlax, R. M. Samelson, and R. A. de Szoeke (2007), Global observations of large oceanic eddies, *Geophys. Res. Lett.*, *34*, L15606, doi:10.1029/2007GL030812.

Chelton, D. B., M. G. Schlax, and R. M. Samelson (2011), Global observations of nonlinear mesoscale eddies, *Prog. Oceanogr.*, *91*(2), 167–216, doi:10.1016/j.pocean.2011.01.002.

Cipollini, P., D. Cromwell, P. G. Challenor, and S. Raffaglio (2001), Rossby waves detected in global ocean colour data, *Geophys. Res. Lett.*, *28*(2), 323–326.

Cordier, E., J. Lézé, and J.-L. Join (2013), Natural tidal processes modified by the existence of fringing reef on La Reunion Island (Western Indian Ocean): Impact on the relative sea level variations, *Cont. Shelf Res.*, *55*, 119–128, doi:10.1016/j.csr.2013.01.016.

de Ruijter, W. P. M., H. Ridderinkhof, and M. W. Schouten (2005), Variability of the southwest Indian Ocean, *Philos. Trans. R. Soc. A*, *363*(1826), 63–76, doi:10.1098/rsta.2004.1478.

Dee, D. P., et al. (2011), The ERA-Interim reanalysis: Configuration and performance of the data assimilation system, *Q. J. R. Meteorol. Soc.*, *137*(656), 553–597, doi:10.1002/qj.828.

Demerliac, A. (1974), Le niveau de la mer. Calcul du niveau moyen journalier, Service Hydrographique et Ocanographique de la Marine, *Ann. Hydrogr.*, *741*, 49–57.

Dong, C., and J. C. McWilliams (2007), A numerical study of island wakes in the Southern California Bight, *Cont. Shelf Res.*, *27*(9), 1233–1248, doi:10.1016/j.csr.2007.01.016.

Dong, C., J. C. McWilliams, and A. F. Shchepetkin (2007), Island wakes in deep water, *J. Phys. Oceanogr.*, *37*(4), 962–981, doi:10.1175/JPO3047.1.

Ferry, N., L. Parent, G. Garric, and C. Bricaud (2012), GLORYS2V1 global ocean reanalysis of the altimetric era (1993–2009) at meso scale, *Mercator Quart. Newsl.*, *22*, 28–39.

Halo, I., B. Backeberg, P. Penven, I. Ansorge, C. Reason, and J. E. Ullgren (2014), Eddy properties in the Mozambique Channel: A comparison between observations and two numerical ocean circulation models, *Deep Sea Res., Part II*, *100*, 38–53.

Jia, F., L. Wu, and B. Qiu (2011), Seasonal modulation of eddy kinetic energy and its formation mechanism in the Southeast Indian Ocean, *J. Phys. Oceanogr.*, *41*(4), 657–665, doi:10.1175/2010JPO4436.1.

Killworth, P., D. B. Chelton, and R. A. de Szoeke (1997), The speed of observed and theoretical long extratropical planetary waves, *J. Phys. Oceanogr.*, *27*, 1946–1966.

Kummerow, C. E. A. (2000), The status of the tropical rainfall measuring mission (TRMM) after two years in orbit, *J. Appl. Meteorol.*, *39*, 1965–1982.

Large, W., and S. Yeager (2004), Diurnal to decadal global forcing for ocean and sea-ice models: The data sets and flux climatologies, Tech. Note NCAR/TN-460+STR, Natl. Center for Atmos. Res., Boulder, Colo.

Lazure, P., and F. Dumas (2008), An external-internal mode coupling for a 3D hydrodynamical model for applications at regional scale (MARS), *Adv. Water Resour.*, *31*(2), 233–250, doi:10.1016/j.advwatres.2007.06.010.

Le Friant, A., E. Lebas, V. Clément, G. Boudon, C. Deplus, B. de Voogd, and P. Bachèlery (2011), A new model for the evolution of La Réunion volcanic complex from complete marine geophysical surveys, *Geophys. Res. Lett.*, *38*, L09312, doi:10.1029/2011GL047489.

Lefevre, F., F. Lyard, and C. Le Provost (2002), FES99: A global tide finite element solution assimilating tide gauge and altimetric information, *J. Atmos. Oceanic Technol.*, *19*, 1345–1356.

Lin, X., Y. Yin, and J. Yang (2014), A mechanism for the latitudinal dependence of peak-spectrum sea surface height variability, *J. Geophys. Res.*, *119*, doi:10.1002/2013JC009642, in press.

Lyard, F., F. Lefevre, T. Letellier, and O. Francis (2006), Modelling the global ocean tides: Modern insights from FES2004, *Ocean Dyn.*, *56*(5–6), 394–415, doi:10.1007/s10236-006-0086-x.

Madec, G. (2008), NEMO ocean engine, Tech. Rep. 27, Institut Pierre-Simon Laplace, France.

Marchesiello, P., L. Debreu, and X. Couvelard (2009), Spurious diapycnal mixing in terrain-following coordinate models: The problem and a solution, *Ocean Modell.*, *26*(3–4), 156–169, doi:10.1016/j.ocemod.2008.09.004.

Marsaleix, P., F. Auclair, and C. Estournel (2009), Low-order pressure gradient schemes in sigma coordinate models: The seamount test revisited, *Ocean Modell.*, *30*(2–3), 169–177, doi:10.1016/j.ocemod.2009.06.011.

Morales, R., E. Barton, and K. Heywood (1996), Variability of water masses in the western Indian Ocean, *J. Geophys. Res.*, *101*(C6), 14,027–14,038.

Morrow, R., and F. Birol (1998), Variability in the southeast Indian Ocean from altimetry: Forcing mechanisms for the Leeuwin Current, *J. Geophys. Res.*, *103*, 18,529–18,544.

Morrow, R., F. Birol, and D. Griffin (2004), Divergent pathways of cyclonic and anti-cyclonic ocean eddies, *Geophys. Res. Lett.*, *31*, L24311, doi:10.1029/2004GL020974.

New, A. L., S. Alderson, D. Smeed, and K. Stansfield (2007), On the circulation of water masses across the Mascarene Plateau in the South Indian Ocean, *Deep Sea Res., Part I*, *54*(1), 42–74, doi:10.1016/j.dsr.2006.08.016.

Palastanga, V., P. J. van Leeuwen, and W. P. M. de Ruijter (2006), A link between low-frequency mesoscale eddy variability around Madagascar and the large-scale Indian Ocean variability, *J. Geophys. Res.*, *111*, C09029, doi:10.1029/2005JC003081.

Palastanga, V., P. J. van Leeuwen, M. W. Schouten, and W. P. M. de Ruijter (2007), Flow structure and variability in the subtropical Indian Ocean: Instability of the South Indian Ocean countercurrent, *J. Geophys. Res.*, *112*, C01001, doi:10.1029/2005JC003395.

Pedlosky, J. (1987), Geophysical Fluid Dynamics, 2nd ed., Springer, New York.

Penven, P., V. Echevin, J. Pasapera, F. Colas, and J. Tam (2005), Average circulation, seasonal cycle, and mesoscale dynamics of the Peru Current System: A modeling approach, *J. Geophys. Res.*, *110*, C10021, doi:10.1029/2005JC002945.

Qiu, B. (1999), Seasonal eddy field modulation of the north pacific subtropical countercurrent: TOPEX/Poseidon observations and theory, *J. Phys. Oceanogr.*, *29*(10), 2471–2486, doi:10.1175/1520-0485(1999)029¡2471:SEFMOT¿2.0.CO;2.

Qiu, B., and S. Chen (2004), Seasonal modulations in the eddy field of the South Pacific Ocean, *J. Phys. Oceanogr.*, *34*(7), 1515–1527, doi:10.1175/1520-0485(2004)034¡1515:SMITEF¿2.0.CO;2.

Qiu, B., and S. Chen (2010), Interannual variability of the north pacific subtropical countercurrent and its associated mesoscale eddy field, *J. Phys. Oceanogr.*, *40*(1), 213–225, doi:10.1175/2009JPO4285.1.

Quartly, G., J. Buck, M. Srokosz, and A. Coward (2006), Eddies around Madagascar: The retroflection re-considered, *J. Mar. Syst.*, *63*(3–4), 115–129, doi:10.1016/j.jmarsys.2006.06.001.

Schott, F., M. Fieux, J. Kindle, J. Swallow, and R. Zantopp (1988), The boundary currents east and north of Madagascar. 2: Direct measurements and model comparisons, *J. Geophys. Res.*, *93*(C5), 4963–4974, doi:10.1029/JC093iC05p04963.

Schott, F. A., and J. P. McCreary (2001), The monsoon circulation of the Indian Ocean, *Prog. Oceanogr.*, *51*(1), 1–123, doi:10.1016/S0079-6611(01)00083-0.

Schouten, M. W., W. P. M. de Ruijter, and P. J. van Leeuwen (2002a), Upstream control of Agulhas Ring shedding, *J. Geophys. Res.*, *107*(C8), 3109, doi:10.1029/2001JC000804.

Schouten, M. W., W. P. M. de Ruijter, P. J. van Leeuwen, and H. A. Dijkstra (2002b), An oceanic teleconnection between the equatorial and southern Indian Ocean, *Geophys. Res. Lett.*, *29*(16), 1812, doi:10.1029/2001GL014542.

Shchepetkin, A. F., and J. C. McWilliams (2003), A method for computing horizontal pressure-gradient force in an oceanic model with a nonaligned vertical coordinate, *J. Geophys. Res.*, *108*(C3), 3090, doi:10.1029/2001JC001047.

Siedler, G., M. Rouault, and J. R. E. Lutjeharms (2006), Structure and origin of the subtropical South Indian Ocean Countercurrent, *Geophys. Res. Lett.*, *33*, L24609, doi:10.1029/2006GL027399.

Sikirić, M. D., I. Janeković, and M. Kuzmić (2009), A new approach to bathymetry smoothing in sigma-coordinate ocean models, *Ocean Modell.*, *29*(2), 128–136, doi:10.1016/j.ocemod.2009.03.009.

Song, Y., and D. B. Haidvogel (1994), A semi-implicit ocean circulation model using a generalized topography-following coordinate system, *J. Comput. Phys.*, *115*, 228–244.

Souza, J. M. A. C., C. de Boyer Montégut, and P. Y. Le Traon (2011), Comparison between three implementations of automatic identification algorithms for the quantification and characterization of mesoscale eddies in the South Atlantic Ocean, *Ocean Sci.*, *7*(3), 317–334, doi:10.5194/os-7-317-2011.

Stramma, L., and J. Lutjeharms (1997), The flow field of the subtropical gyre of the South Indian Ocean, *J. Geophys. Res.*, *102*(C3), 5513–5530.

Umlauf, L., and H. Burchard (2003), A generic length-scale equation for geophysical turbulence models, *J. Mar. Res.*, *61*, 235–265.

Warren, B. A., T. Whitworth, and J. H. LaCasce (2002), Forced resonant undulation in the deep Mascarene Basin, *Deep Sea Res., Part II*, *49*(7–8), 1513–1526, doi:10.1016/S0967-0645(01)00151-5.

Weijer, W. (2008), Normal modes of the Mascarene Basin, *Deep Sea Res., Part I*, *55*(1), 128–136, doi:10.1016/j.dsr.2007.10.005.